Effect of Virtual Mass and Time Delay on the Stability of Haptic Rendering

Ahmad Mashayekhi, Mehdi Shakeri, Amin Khorasani, and Tom Verstraten, *Member, IEEE*

***Abstract*—Virtual mass simulation is one of the recent topics in the field of haptic devices (HDs), which can alter the apparent mass of the HD. Simulating negative values of virtual mass leads to a decrease in the apparent effective mass, improving transparency but weakening stability. Positive virtual mass rendering increases the apparent mass, reduces transparency, and enhances stability. This paper analyzes the stability of a haptic device while simulating a virtual environment consisting of a mass, spring, and damper in the presence of a constant time delay. The results are closed-form equations that can predict the stability boundary for small and even large values of virtual damping and time delay. These closed-form equations demonstrate that the maximum renderable virtual mass is twice the physical mass of the HD, and the minimum value equals its negative; both occur in the case of zero time delay. Increasing the time delay reduces both the minimum and maximum values of the renderable virtual mass. The study also shows that using virtual mass can improve the maximum value of a renderable virtual spring. The equations show that, in the absence of delay, properly tuning the virtual mass and virtual damping can enlarge the maximum renderable stiffness by up to 5.8 times in theory. In the experiments under time delay, the stiffness increased by a factor of 3.5, compared to the theoretical prediction of 4.1 times. The results further reveal situations where a nonzero *minimum* stiffness is required for stability. All findings are validated via simulations and experiments on a dedicated test bed.**

***Index Terms*—Haptic device (HD), stability, virtual mass, time delay.**

I. Introduction

A HAPTIC device (HD) is a robot that can be used for simulating virtual environments (VEs) [1], teleoperation [2], [3], [4], and learning from demonstration [5]. HDs are designed to transmit virtual forces and torques to users with the highest level of transparency. In this way, the HD enables users to physically interact with the VE, providing a sense of reality and tangibility.

Rendering inertia and inertial forces can enhance the sense of touch and the experience of VEs. Employing negative values for virtual inertia, or mass, may reduce the impact of reflected inertia on the operator's side. Minimizing reflected inertia enhances the transparency of haptic devices, but it can also lead to instability [6]. Based on the results of this work and previous studies such as [6], [7], [8], it can be stated that in cases where the virtual environment includes mass, simulating positive virtual mass values can boost the maximum renderable stiffness before the system becomes unstable.

Haptic devices typically have several degrees of freedom (DOF) and can be configured in either series or parallel arrangements. Due to their multi-DOF, nonlinear, and intricate dynamics, it is challenging — if not impossible — to use these dynamics directly in stability and passivity analysis. When simulating a virtual environment, the haptic device's end-effector, known as the stylus, makes limited movements around its operating point. This allows the complex and nonlinear dynamics of the haptic device to be simplified into a 1-DOF system consisting of an effective mass, viscous friction, and Coulomb friction, operating with an effective sensor resolution, as shown in [9].

The main contribution of this paper is the development and derivation of closed-form stability equations and boundaries for haptic devices operating in virtual environments modeled as mass-spring-damper systems with time delay, virtual damping, and virtual mass, providing useful theoretical insights for haptic rendering. In contrast to previous studies, which were valid only for the case of no time delay and relied on trial-and-error approaches to define stability ranges, this work presents an explicit mathematical relationship. It connects the physical parameters of haptic devices to the virtual environment parameters, as well as to the time delay. The proposed equations are versatile, covering both small and large values of time delay, virtual damping, and virtual mass. Novelties are therefore observed both in the absence and in the presence of a time delay. In the absence of time delay, the closed-form analysis shows that introducing virtual mass can, in theory, significantly increase the maximum renderable stiffness. In fact, it is shown that the maximum theoretical value of the virtual stiffness can be increased by up to 5.8 times by adding virtual mass and tuning the virtual damping. When time delay is included, the stability boundaries can still be obtained efficiently, and the behavior of the haptic device can be systematically analyzed. In this delayed case, it is shown that adding virtual mass can increase the maximum renderable stiffness by about 4.1 times theoretically, which is consistent with the 3.5-fold increase observed in the experiments. In addition, the findings indicate that—whether time delay exists or not—in certain cases, a non-zero minimum value for the virtual spring

Received 22 May 2025; revised 16 October 2025 and 25 November 2025; accepted 6 December 2025. This work was supported by Research Foundation Flanders (FWO) SBO-ELYSA Project under Grant S001821N. This article was recommended for publication by Associate Editor H. Singh and Editor-in-Chief J.-H. Ryu upon evaluation of the reviewers' comments. *(Corresponding author: Ahmad Mashayekhi.)*

Ahmad Mashayekhi, Amin Khorasani, and Tom Verstraten are with BruBotics, Vrije Universiteit Brussel, 1050 Brussels, Belgium, and also with Flanders Make, Brussels, Belgium (e-mail: Ahmad.Mashayekhi@vub.be).

Mehdi Shakeri is with the University of Regina, Regina, SK S4S 0A2, Canada.

Digital Object Identifier 10.1109/TOH.2025.3642614

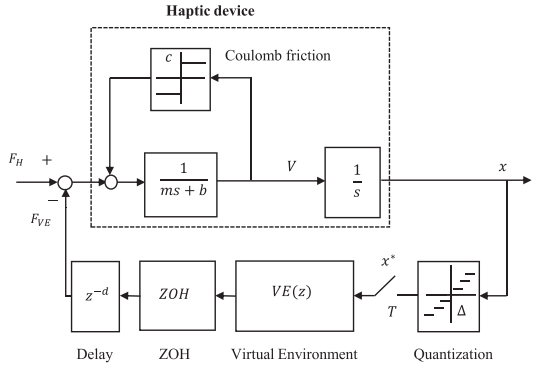

Fig. 1. The 1-DOF nonlinear model of a haptic device.

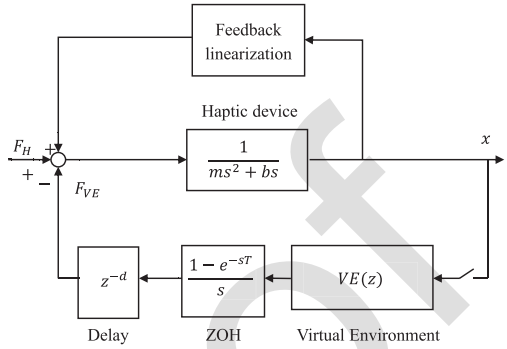

Fig. 2. Linear model of the haptic device. In the experimental setup used in this paper, the Coulomb friction and gravity torque are compensated in the feedback linearization block.

is required for stability, a phenomenon not reported in previous studies. These improvements arise because, unlike earlier works, our analysis is not restricted to the zero-delay case with positive values of virtual damping and is based on closed-form derivations rather than trial-and-error methods. These findings verify that the proposed framework remains valid under delayed conditions and establish a new analytical approach that has not been reported before.

The structure of the paper is as follows: a review of previous analyses is presented in Section II, while Section III contains the modeling of the HD. Stability analysis and the derivation of the stability boundary equations are presented in Section IV. Simulations and experiments are conducted and reported in Sections V and VI, respectively. Section VII presents the results and discusses them. The paper concludes with the conclusions and references sections.

II. Previous Analyses

Although the HDs may exhibit multi-DOF nonlinear dynamics, in [9] and [10], closed-form equations are provided to calculate the values of the effective mass, viscous friction, Coulomb friction, and resolution of a multi-DOF HD as functions of its dynamic parameters and operating point. The accuracy of these equations in predicting the stability boundary is also evaluated and discussed, showing good agreement between the original nonlinear multi-DOF system and the new simplified 1-DOF model. Based on these findings, the nonlinear schematic view of the HD is presented in Fig. 1. In this figure, m, b, c, and Δ represent the effective mass, viscous friction, Coulomb friction, and resolution, respectively, and are used in many theoretical analyses such as [11]. Due to the discrete nature of the HD, the position of the stylus (x) is sampled with a constant sampling time of T and used within the virtual environment $VE(z)$. This force is passed through a zero-order hold and a time delay of T_d, and then applied to the HD by its actuators as the virtual environment force (F_{VE}). This force is added to the operator's hand force (F_H).

A simplified linear model of the HD is shown in Fig. 2. This model includes only linear phenomena and is applicable when Coulomb friction and quantization are negligible. Additionally, previous studies [11], [12], [13] have demonstrated that Coulomb friction can dissipate the energy introduced by quantization. Some phenomena, such as possible saturation and quantization in the actuators or internal vibration modes of the interface, are not considered. Although user dynamics are also involved in the loop, their influence generally enhances system stability [14], [15], [16]. Therefore, these dynamics have not been included in the block diagram, which can be regarded as a simplified and worst-case scenario.

Under these assumptions, the linear model can serve as a good approximation for determining stability conditions. This approach has been widely used in various studies for stability and passivity analysis in HDs, such as [7], [8], [9], [14], [17], [18], [19].

Colonnese et al. identified important parameters for system passivity and stability, presented passivity and stability boundaries, predicted noise limit cycles and established conditions for their existence, and described the expected accuracy of rendered virtual mass for a 1-DOF HD [20]. They considered only the virtual mass to simulate the VE, without including the virtual spring and damper. Desai et al. studied the effect of virtual mass simulation on the maximum achievable virtual stiffness of a 1-DOF HD [21]. They showed that the maximum value of the virtual stiffness is achieved when the virtual mass equals the effective mass of the HD. Furthermore, they demonstrated that the maximum stiffness obtained by simulating virtual mass is about 2.5 times higher than that achievable with virtual damping. However, they did not consider time delay in their research, even though time delay is one of the key parameters significantly affecting system performance and stability.

Stability analysis of a 1-DOF HD with different combinations of mass, spring, and damper is studied in [6], in the case of no time delay, by applying the Routh-Hurwitz criterion to the characteristic equation of the closed-loop system. For this purpose, in the absence of time delay, they introduced a set of nonlinear inequalities through which the stability boundary could be determined using numerical methods and iterative procedures. Gil et al. analyzed the effect of implementing virtual inertia/mass on the stability of a 1-DOF HD in the case of zero time delay [17]. They proposed a method to measure the physical inertia of their haptic device and thus characterize its dynamics. Additionally, they examined how position filtering (used to mitigate excessive

IEEE Transactions on Haptics (ToH) paper, presented at ICRA 2026, Vienna, Austria. Cite as ToH paper.

TABLE I
DIMENSIONLESS PARAMETERS

Parameter	Variable	Dimensionless variable
Sampling time	T	-
Time delay	T_d	$d = T_d/T$
Physical mass	m	-
Physical damping	b	$\delta = bT/m$
Virtual stiffness	K_w	$\alpha = K_w T^2/m$
Virtual damping	B_w	$\beta = B_w T/m$
Virtual mass	M_w	$\gamma = M_w/m$

noise in acceleration calculations) influences stability. However, the study was limited to a zero-time delay, and virtual damping was not included (the virtual environment consisted of only a mass and spring, without a damper). Another limitation is that even without time delay and virtual damping, numerical methods were employed to determine and visualize the stability boundary, as closed-form equations were not used for this purpose.

Researchers have simulated a VE consisting of only a mass (without spring and damper) [8], where time delay was not considered, and no closed-form equations were derived. The use of virtual mass rendering as a means of dissipating energy to stabilize the haptic system has been studied in [7]. According to their results, while energy dissipation through virtual damping is ineffective at high speeds, virtual mass can still dissipate energy efficiently even at high velocities. Recently, this concept was employed in studies such as [22] to enhance the stability boundary of a 7-DOF human upper limb exoskeleton.

III. MODELING

The model of the HD depicted in Fig. 2 is used to calculate the stability boundaries. The VE is assumed to be a bilateral wall consisting of a virtual spring of K_w, virtual damping with a damping coefficient of B_w, and a virtual mass of M_w. Due to the discrete nature of the HD, these parameters are modeled in the discrete domain. Therefore, the transfer function of the VE in the z-domain is given as follows:

$$VE(z) = K_w + B_w \frac{z-1}{Tz} + M_w \frac{(z-1)^2}{T^2 z^2}, \tag{1}$$

where T is a constant number and represents the sampling time.

Time delay may exist in a haptic system due to various sources such as force calculation, communication, or motor control. Given the typically fast sampling rates of HDs, even a few milliseconds of delay correspond to several sampling periods. In HDs with smaller sampling times—such as the Delta and Omega devices with 0.33 ms, or the Impulse Engine with 0.2 ms [11]—the effect of time delay becomes more significant. In stability analysis, it is feasible to treat the aggregate of all delays within the control loop as a single delay represented by T_d[23]. Hence, a constant time delay is defined as the total sum of all delays within the control loop.

To simplify the analysis and reduce the number of variables, dimensionless parameters, as listed in Table I, are used.

IV. STABILITY ANALYSIS

In this section, stability analysis is performed, and closed-form equations are derived to predict the stability boundary of the HD. For this purpose, the closed-loop control system shown in Fig. 2 is used, assuming a discrete virtual environment as described in (1). The ZOH block represents the transfer function of the zero-order hold, and $G(s)$ is the transfer function of the HD.

In this system, the characteristic equation of the system is

$$\Delta = 1 + VE(z)\, z^{-d}\, \mathcal{Z}[\text{ZOH}\, G(s)] = 0, \tag{2}$$

where $\mathcal{Z}$ stands for the z-transformation. Since a zero-order hold is used, $\mathcal{Z}[\text{ZOH}\, G(s)]$ is simplified as

$$\mathcal{Z}[\text{ZOH}\, G(s)] = \mathcal{Z}\left[\frac{1-e^{-Ts}}{s}\frac{1}{ms^2+bs}\right]. \tag{3}$$

Or:

$$\mathcal{Z}[\text{ZOH}\, G(s)] = \frac{\left(e^{-\frac{bT}{m}} - 1 + \frac{bT}{m}\right) z + 1 - \left(1+\frac{bT}{m}\right) e^{-\frac{bT}{m}}}{\frac{(z-1)b^2}{m}\left(z - e^{-\frac{bT}{m}}\right)}. \tag{4}$$

The parameters are assumed to be dimensionless, as defined in Table I, with $\Gamma = e^{\delta}$. Thus, the characteristic equation is simplified in dimensionless form as follows:

$$\begin{aligned}\Delta = {} & \Gamma\delta^2 z^{d+4} - (1+\Gamma)\delta^2 z^{d+3} + \delta^2 z^{d+2} \\ & + [\alpha(1+\Gamma(\delta-1)) + \beta\delta\Gamma \\ & + \gamma(1-\Gamma(1+\delta)) + \delta(1-\Gamma)]z^3 \\ & - [\alpha(1+\delta-\Gamma(1-2\gamma)) + \beta(\Gamma(\gamma-2)+\delta) \\ & + \gamma(3(1-\Gamma)+\delta) + 2\delta]z^2 \\ & + (\alpha\gamma\Gamma + \beta(\gamma-\Gamma) + \gamma(3(1-\Gamma)+2\delta) + \delta)z \\ & - \gamma(1-\Gamma+\delta) = 0.\end{aligned} \tag{5}$$

The roots of the characteristic equation correspond to the poles of the closed-loop system. For the system to be stable, all these roots must lie within the unit circle in the complex z-plane. Accordingly, the stability boundary can be determined by substituting z using the following expression:

$$z = 1e^{j\theta} = \cos(\theta) + j\sin(\theta) \tag{6}$$

Here, j represents the imaginary unit, and θ denotes the complex argument (also known as the angle or phase) in radians. By substituting z from (6) into the characteristic equation in (5) and simplifying, the resulting expression can be separated into real and imaginary components, both of which must independently equal zero for stability($\Re\{X(z)\} + j\Im\{X(z)\} = 0$). The detailed forms of these real and imaginary parts are provided in subsection A of the Appendix. As a result, this approach yields two independent equations, which can be solved for α and β, resulting in the following set of dimensionless parameters:

$$\begin{cases} \alpha = \frac{\gamma C_1 + \gamma\delta^2 C_2 + \gamma\delta C_3 + \delta^3 C_4 + \delta^2 C_5}{C_6 + \delta^2 C_7 + \delta C_8} \\ \beta = \frac{-\gamma C_1 - \gamma\delta^2 C_2 + \gamma\delta C_9 + \delta^3 C_{10} + \delta^2 C_{11}}{C_6 + \delta^2 C_7 + \delta C_8} \end{cases} \tag{7}$$

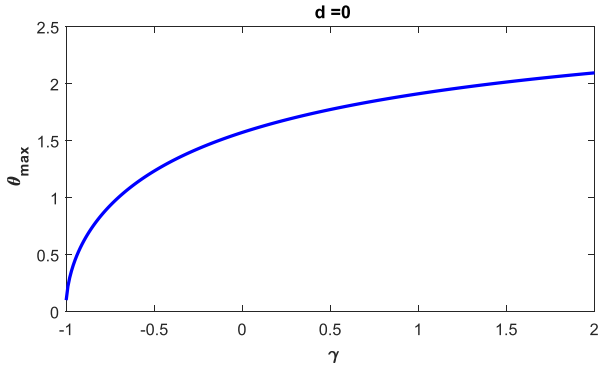

Fig. 3. Plot of $\theta_{\max}$ versus γ in the case of $d = 0$.

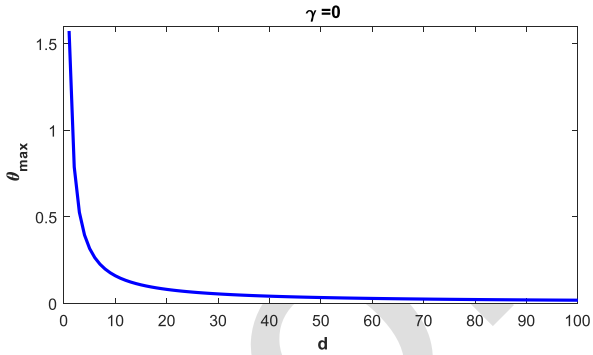

Fig. 4. Plot of $\theta_{\max}$ versus d in the case of $\gamma = 0$.

where $C_i, i = 1, \ldots, 11$ are coefficients listed in the Appendix, subsection B. The above equations can predict the stability boundary without limitations on time delay and virtual damping. In the following subsections, this equation is simplified for some special cases, and equations for the maximum and minimum values of θ are determined and presented.

A. No Time Delay, Arbitrary Virtual Mass

In the case of no time delay (i.e., $d = 0$), the coefficients C_4, C_5, C_{10}, and C_{11} can be simplified, and the stability boundary in (7) can be plotted by varying θ from 0 to its maximum value $\theta_{\max}$, as derived in Appendix C.

$$\theta_{\max} = 2 \arctan\left(\sqrt{\frac{u}{2-u}}\right), \tag{8}$$

where

$$u = -\frac{(1-\Gamma)^2 \delta^2 (\gamma + 1 + \delta)}{2A}, \tag{9}$$

with

$$A = \gamma\left[(1-\Gamma)^2 - \delta(\Gamma^2 - 1) + \Gamma\delta^2\right] + \Gamma\delta^2(1 - \Gamma + \delta). \tag{10}$$

By selecting an appropriate value of γ and using the known HD parameters, the interval $\theta \in [0, \theta_{\max}]$ from (8) can be directly substituted into (7), allowing the entire stability curve to be obtained quickly in closed form, without iteration. As seen in the literature, this case was previously studied in several references, such as [6]. However, the method in [6] requires calculating α on the stability boundary by iteratively searching for the maximum renderable stiffness that satisfies an inequality for each value of γ and β. Therefore, unlike previous, the present formulation provides a direct closed-form approach to generate the complete stability boundaries.

Using (8), the value of $\theta_{\max}$ is plotted for different values of $\gamma \in [-1, 2]$, as shown in Fig. 3. For this purpose, a 1-DOF haptic device with mechanical properties $T = 1\,\text{ms}$, $m = 0.0128\,\text{kg·m}^2$, and $b = 0.0324\,\text{N·m·s/rad}$ (as per the experimental setup in this study) is considered. From Fig. 3, it can be seen that increasing γ causes $\theta_{\max}$ to increase continuously.

B. No Virtual Mass, Arbitrary Time Delay

In the absence of virtual mass (i.e., $M_w = 0$), γ becomes zero, and the general stability equations in (7) simplify to (11).

$$\begin{cases} \alpha = \frac{\delta^3 C_4 + \delta^2 C_5}{C_6 + \delta^2 C_7 + \delta C_8} \\ \beta = \frac{\delta^3 C_{10} + \delta^2 C_{11}}{C_6 + \delta^2 C_7 + \delta C_8} \end{cases} \tag{11}$$

In this case, θ varies from 0 to a new maximum value. When the time delay is zero, this $\theta_{\max}$ is obtained from (8). For nonzero time delay, θ lies within the interval $[0, \theta_{\max}]$, where $\theta_{\max}$ is determined as follows (see Subsection D of the Appendix):

$$\theta_{\max} = \theta_0 - \frac{A_{S0} + A_{D0}\cos(\theta_0)}{A'_{S0} + A'_{D0}\cos(\theta_0) + dA_{D0}\sin(\theta_0)}, \tag{12}$$

where

$$\begin{aligned} \theta_0 &= \frac{\pi}{2(d+1)} \\ A_S(\theta) &= 2\delta\Big(\Gamma^2 + 1 - (\Gamma+1)^2 c + 2\Gamma c^2\Big) \\ &\quad - 4\, sh^2 (\Gamma - 1)\big(1 + \Gamma - 2\Gamma c\big), \\ A_D(\theta) &= -4\, sh^2 (\Gamma - 1)^2, \end{aligned} \tag{13}$$

with $s_h = \sin\frac{\theta}{2}$ and $c = \cos\theta$. The prime symbol ($'$) denotes differentiation with respect to θ, and the subscript "0" indicates that the parameter is evaluated at $\theta = \theta_0$.

For the given physical parameters of the HD, $\theta_{\max}$ is calculated from (47) for different values of $d \in [0, 100]$, as shown in Fig. 4. The figure shows that increasing the time delay reduces $\theta_{\max}$ when γ is kept constant.

C. No Virtual Mass, No Time Delay

In the special case of $d = 0$ and $\gamma = 0$, the stability equation simplifies to the following form:

$$\begin{cases} \alpha = \frac{\delta \sin^2\left(\frac{\theta}{2}\right)\left[\delta^2\left(\Gamma^2 - 2\cos(\theta)\Gamma + 1\right) - \delta(\Gamma-1)(\Gamma - 2\cos(\theta)\Gamma + 1)\right]}{\frac{1}{4}\delta^2(\Gamma^2 - 2\cos(\theta)\Gamma + 1) - \delta\sin^2\left(\frac{\theta}{2}\right)(\Gamma^2 - 1) + \sin^2\left(\frac{\theta}{2}\right)(\Gamma-1)^2} \\ \beta = \frac{-\delta^3\left(\Gamma^2 - 2\cos(\theta)\Gamma + 1\right) + 4\delta^2\sin^2\left(\frac{\theta}{2}\right)\Gamma(\Gamma-1)}{\delta^2(\Gamma^2 - 2\cos(\theta)\Gamma + 1) - 4\delta\sin^2\left(\frac{\theta}{2}\right)(\Gamma^2-1) + 4\sin^2\left(\frac{\theta}{2}\right)(\Gamma-1)^2} \end{cases} \tag{14}$$

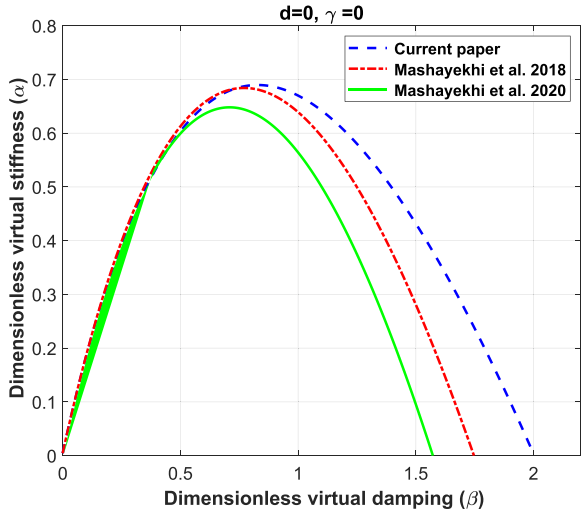

Fig. 5. Dimensionless stability boundary of a haptic device, determined from the current paper ((14)) in dashed blue line, Mashayekhi et al. 2018 (reference [24]) red dotted line, and Mashayekhi et al. 2020 (reference [15]) green solid line.

In this case, $\theta_{\max}$ is obtained by substituting $\gamma = 0$ into (8), as shown in the following equation:

$$\theta_{\max} = 2\arctan\left(\sqrt{\frac{(\Gamma-1)^2(1+\delta)}{4\Gamma(\Gamma-1-\delta)-(\Gamma-1)^2(1+\delta)}}\right). \tag{15}$$

A comparison of the stability boundaries from (14) and the previous results in [15], [24] is shown in Fig. 5. Using (14), $\theta_{\max} = 1.5725$ rad is obtained, whereas the alternative methods yield a frequency of $\omega_{\max} = 1572.4$ rad/s. From Fig. 5, it can be seen that all three different methods have the same starting point. In fact, in [15], [24] it is shown that, for all values of time delay, the minimum dimensionless virtual damping is $\beta_{\min} = -bT/m$. Moreover, in the following sections, it is shown that for all values of time delay and virtual mass, the minimum value of β remains the same. Despite having the same starting point, the endpoints of the curves vary significantly. For $d = 0$, both (7) and (14) lead to $\beta_{\max} = 2$, which is the correct result and is fully consistent with prior studies [6], [18], [19], [21].

In the general case where both time delay and virtual mass are present, determining $\theta_{\max}$ in a closed-form expression is a challenging task. Since the presence of time delay reduces $\theta_{\max}$, assuming $d = 0$ provides an upper bound for its value. The actual value of $\theta_{\max}$ can then be obtained numerically, lying between zero and this upper bound.

In Subsection E of the Appendix, it is shown that for stability, it is necessary to have $\alpha > 0$, and that all stability boundaries start from the same point, $(B_w, K_w) = (-b, 0)$, or, in dimensionless form, $(\beta, \alpha) = (-\delta, 0)$, regardless of the values of time delay and virtual mass. This result is consistent with the case of simulating a virtual environment consisting solely of a virtual spring and damper, as previously demonstrated in [14], [18], [19], [24], [25]. However, the maximum value of β is influenced by various factors, such as d and γ.

V. Simulations

This section presents a series of simulations comparing the theoretical stability boundaries obtained from (7) with those derived using MATLAB/Simulink, based on the previously mentioned physical parameters of the HD. The virtual environment is modeled as a discrete version of (1), with a zero-order hold block used in the simulations. Various time delays $T_d = [0, 1, 5, 10] \times T$ and both positive and negative values of virtual mass are considered. First, the values $\gamma = [0, -0.25, -0.5, -0.75]$ are selected, and the theoretical stability boundaries are calculated using (7) and compared with the highlighted stability regions obtained from simulations, as shown in Fig. 6.

To generate the highlighted areas corresponding to the simulation-based stability results, the theoretical stability boundary is first determined using the analytical model in (7). Then, the α and β parameter spaces are uniformly discretized into $N \times N$ intervals (mostly $N = 100$), and for each pair (β, α), a simulation is performed to evaluate the stability of the haptic device. Stable operating points are identified and collectively used to form the highlighted stable regions, which are subsequently compared with the theoretical stability boundaries.

As seen in Fig. 6, the simulation results align with the theoretical predictions for both small and large time delays (d) and negative values of the virtual mass (γ). Both sets of results indicate that when $\alpha < 0$, no stability boundary exists, a result that was previously observed theoretically.

Additionally, it can be observed that using negative values of γ reduces the stability region, regardless of the time delay. Specifically, for $\gamma \leq 0$, the smaller the value of γ, the narrower the stability region becomes. Both theoretical and simulation results indicate that when $\gamma \leq -1$, the stability region vanishes entirely.

At $\gamma = -1$, the reflected inertia at the HD output becomes zero, effectively making the HD appear to have no mass. Thus, completely eliminating reflected inertia is not feasible. In this case, the theoretical stability boundary begins with a zero slope (unlike the positive slope observed for $-1 < \gamma < 0$) and extends into negative α values, representing an unstable region

All theoretical stability curves commence at $\beta_{\min} = -bT/m = -0.00253$. The maximum value of β is determined by the values of α, γ, and d. In Fig. 6(a), the maximum value of β, $\beta_{\max} = 2$, is observed in the specific case where $d = 0$ and $\gamma = 0$. However, as the time delay increases and the virtual mass decreases, the maximum achievable value of β is correspondingly reduced.

It is important to note that the time delay T_d does not alter the intrinsic physical parameters of the haptic device, namely the robot mass m and damping b. These parameters appear only through $\delta = bT/m$ and $\Gamma = e^{\delta}$, which are independent of T_d. Instead, the effect of the delay is embedded in the trigonometric terms involving $d = T_d/T$ within the coefficients C_4, C_5, C_{10}, and C_{11} in (7). These terms distort the effective contributions of the virtual environment parameters (α, β, and γ) in the stability condition. As a result, increasing the delay reduces the stability region by shrinking the set of admissible values for the virtual stiffness, damping, and mass, even though the physical device

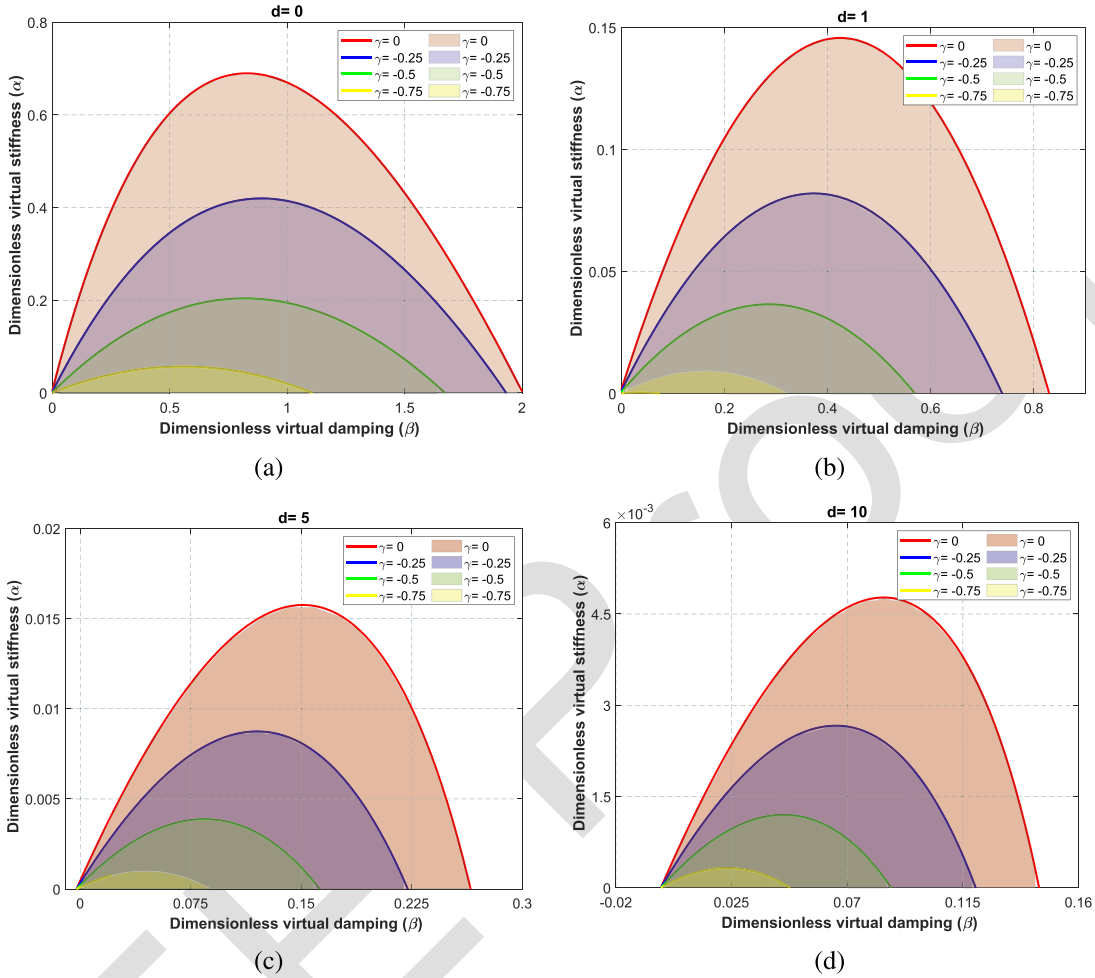

Fig. 6. The theoretical stability boundaries (solid lines, determined from (7)) versus stability regions determined by simulations (highlighted areas) for different virtual masses (γ) and different dimensionless time delays of: (a) $d = 0$, (b) $d = 1$, (c) $d = 5$, and (d) $d = 10$. It can be seen that the stability regions decrease significantly with increasing time delay (d). Changing the scales would make the figures for higher d too small, so all figures are fitted to their current axes.

itself remains unchanged. This explains why the renderable stiffness decreases with delay and provides a clear physical interpretation of the stability boundaries shown in the results.

For positive values of virtual mass, the stability curves exhibit distinctive shapes. Fig. 7 illustrates the stability boundaries for $d = 0$ with various positive values of γ, ranging from 0 to 3.

According to Fig. 7, for $\gamma < 2$, the stability curves begin at the point $(\alpha, \beta) = (0, \beta_{w_{\min}})$ on the $\alpha - \beta$ plane and extend to the right, forming right-sided curves. Simulations in the following paragraphs verify that the regions beneath these right-sided curves are stable, denoted by the letter 'S' in their legend.

For $\gamma > 2$, the stability curves start from the same point but extend to the left, forming left-sided curves. It will be shown in the following paragraphs that the regions beneath these curves are unstable, marked by the letter 'U'. At $\gamma = 2$, the stability curve forms a straight line starting from the same point, and it neither curves to the right nor left, representing the boundary of stability. This case is denoted by the letter 'B' in the legend.

There are several significant coordinates in this graph, marked with black circles numbered from 1 to 6. The first circle, labeled as 1, represents the maximum value of α when there is no virtual mass ($\gamma = 0$). At this point, the maximum value of α is $\alpha_{\max} = 0.6896$, which occurs at $\beta = 0.8206$. This maximum value of α is consistent with results of [6], [21]. Fig. 7 illustrates that, under the assumption of no virtual damping and no virtual mass ($\gamma = 0$ and $\beta = 0$), a very small value of $\alpha = 0.005$ can be achieved. (This point is not shown in the figure, as it is located very close to the origin.) However, with the same value of $\beta = 0$, increasing γ from 0 to $\gamma = 1$ allows for an achievable value of $\alpha = 2$ (indicated by circle 2in Fig. 7). This demonstrates the effect of increasing the virtual mass in enhancing the maximum renderable stiffness.

In scenarios without time delays, a dimensionless virtual spring value greater than 2 can be achieved by selecting specific parameter values. For instance, with $\beta = -1$ and $\gamma = 1.5$, a value of $\alpha \approx 3$ is attainable (indicated by circle 3in Fig. 7).

The maximum *theoretically* renderable value of $\alpha_{\max} \approx 4$ can be achieved with $\beta = -2$ and $\gamma = 2$ under the assumption of no time delay (indicated by circle 4 in Fig. 7). Comparing this with $\alpha_{\max} = 0.6896$ (obtained with $\gamma = 0$), an approximately 5.8-fold increase is observed. It is important to note that reaching this point requires very precise tuning of β and γ, as the stability region near this point is quite narrow. It should be noted that this increase in $\alpha_{\max}$ will decrease when a time delay is introduced,

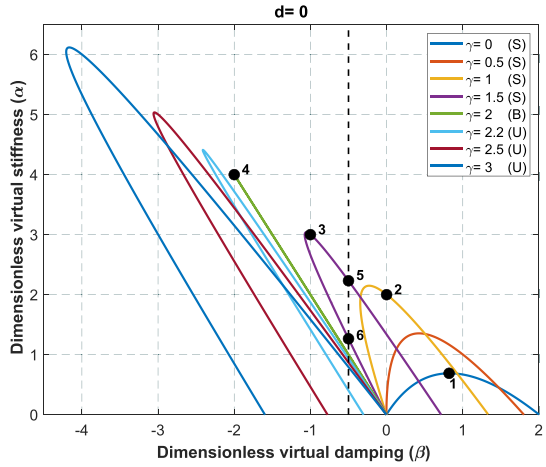

Fig. 7. Stability boundaries of the HD for different values of virtual mass with no time delay. In the case of $\gamma < 2$, the HD is stable (denoted by *S*), while for $\gamma > 2$, it is unstable *(U)*. The value of $\gamma = 2$ yields being on the boundary of stability *(B)*. Important coordinates are depicted by numbered circles and the vertical dashed line.

as demonstrated in the experiments and further detailed in the Results and Discussion section.

Another noteworthy observation regarding the behavior of the HD's stability is presented in Fig. 7, specifically for the case of $\gamma = 1.5$. It can be seen that, at $\beta = -0.5$ (indicated by the vertical black dashed line), there are two significant points within the graph. The first is the maximum renderable value of α, marked by circle 5. The second is the minimum required α for stability, indicated by circle 6. This suggests that, in certain scenarios, a minimum virtual stiffness is necessary for stable haptic rendering. In contrast, when rendering only virtual springs and dampers, this minimum stiffness was not required and was always zero. This behavior, which has not been reported in the reviewed literature, will be further validated through simulations and experiments in the subsequent sections.

It should be noted that the stability regions reported in [6] represent a subset of those shown in Fig. 7. In fact, the stability analysis in that reference was performed only within the range $\beta, \gamma \in [0, +2]$, resulting in a limited portion of the full stability map shown in Fig. 7. If the formulations presented in [6] are applied over the extended ranges $\alpha \in [0, +4], \beta \in [-2, +2]$, and $\gamma \in [-1, +2]$, and $\alpha_{\max}$ is found iteratively for each value of β and γ while sweeping these parameters through their ranges, the obtained stability regions become fully consistent with those presented in this paper, as shown in Fig. 7. This confirms the consistency of the results presented in the current paper and highlights the advantage of using closed-form equations to predict the stability boundaries more efficiently.

Based on the behavior of the stability boundaries observed in Fig. 7, different time delays, specifically $d = [0, 1, 5, 10]$, are selected, and various values of $\gamma = [0, 0.5, 1, 1.5, 2, 2.2]$ are considered. The stability boundaries are predicted using (7) and then verified through simulations, as shown in Fig. 8. All highlighted areas with different colors are obtained from simulations.

According to Fig. 8(a), for $\gamma < 2$, all stability boundaries determined by (7) form right-sided curves, indicating stable behavior, which is also verified by simulations. In the case of $\gamma = 2$, the HD lies on the boundary of stability, with the curve being neither right-sided nor left-sided. For $\gamma > 2$, the stability boundaries become left-sided, indicating unstable behavior of the HD. Consequently, no stable region is observed in the simulation results for these cases.

It should be emphasized that, when these curves were first obtained, simulations were initially performed to determine which side of the boundary was stable, since this behavior had not been reported in the literature before (particularly for $\gamma > 2$). The results confirmed that the regions beneath the right-sided curves are stable, whereas those beneath the left-sided curves are unstable. With this understanding, simulations are no longer required for classification: right-sided curves always represent stable regions, left-sided curves correspond to unstable regions, and the case of $\gamma = 2$ defines the boundary itself.

In the case of $d = 1$, Fig. 8(b) shows that the cases of $\gamma = 2$ (which was the stability boundary for $d = 0$) and $\gamma = 1.5$ (which was stable for $d = 0$) are now left-sided curves and, therefore, unstable. This instability occurs due to the introduction of the time delay. All other cases are right-sided and, therefore, stable, which is precisely verified by simulations (colored regions).

By increasing the time delay to $d = 5$ and $d = 10$, in the case of $\gamma = [0, 0.5, 1]$, the stability boundaries determined by (7) remain right-sided and, therefore, stable, as verified by simulations, as shown in Fig. 8(c) and (d). All other cases remain left-sided, indicating instability in the HD.

In Fig. 8, from (a) to (d), it is evident that increasing the time delay leads to instability in the HD and compresses the stability regions. On the one hand, increasing γ helps simulate higher values of α; on the other hand, it narrows the stability region and can even cause it to become a line, as seen in Fig. 8(a) when γ changes from 0 to 2.

In certain cases in Fig. 8, a minimum virtual stiffness is required for the stability of rendering virtual mass, whereas for $\gamma = 0$, no virtual stiffness is needed.

By comparing the stability boundaries for both positive and negative values of the virtual mass (i.e., Figs. 6 and 8), it can be observed that, on the one hand, the maximum value of β is 2, and on the other hand, this value can be achieved when $d = 0$ and $\gamma = 0$.

From Figs. 6, 7, and 8, it can be seen that all starting points of the stability boundaries are almost the same $(\beta, \alpha) = (-bT/m, 0)$, regardless of the values of d and γ.

VI. Experiments

Experiments have been conducted to validate the derived stability equations. For this purpose, a 1-DOF haptic device equipped with a *MaxonECi-52* motor is actively controlled to simulate the virtual object on its paddle side (Fig. 9). On the paddle side, the haptic device has an inertia of $0.0128\,\mathrm{Kg}\cdot\mathrm{m}^2$, while its viscous and Coulomb frictions have been identified as $0.0324\,\mathrm{N}\cdot\mathrm{m}\cdot\mathrm{s/rad}$ and $0.0318\,\mathrm{N}\cdot\mathrm{m}$, respectively ([26], [27]). A 3-channel incremental encoder with 4096 pulses per revolution improves the resolution to better than 3 seconds after quadrature and gear train for reading the paddle angle. The Coulomb friction and gravity torque are compensated in the feedback linearization block depicted in Fig. 2. During the

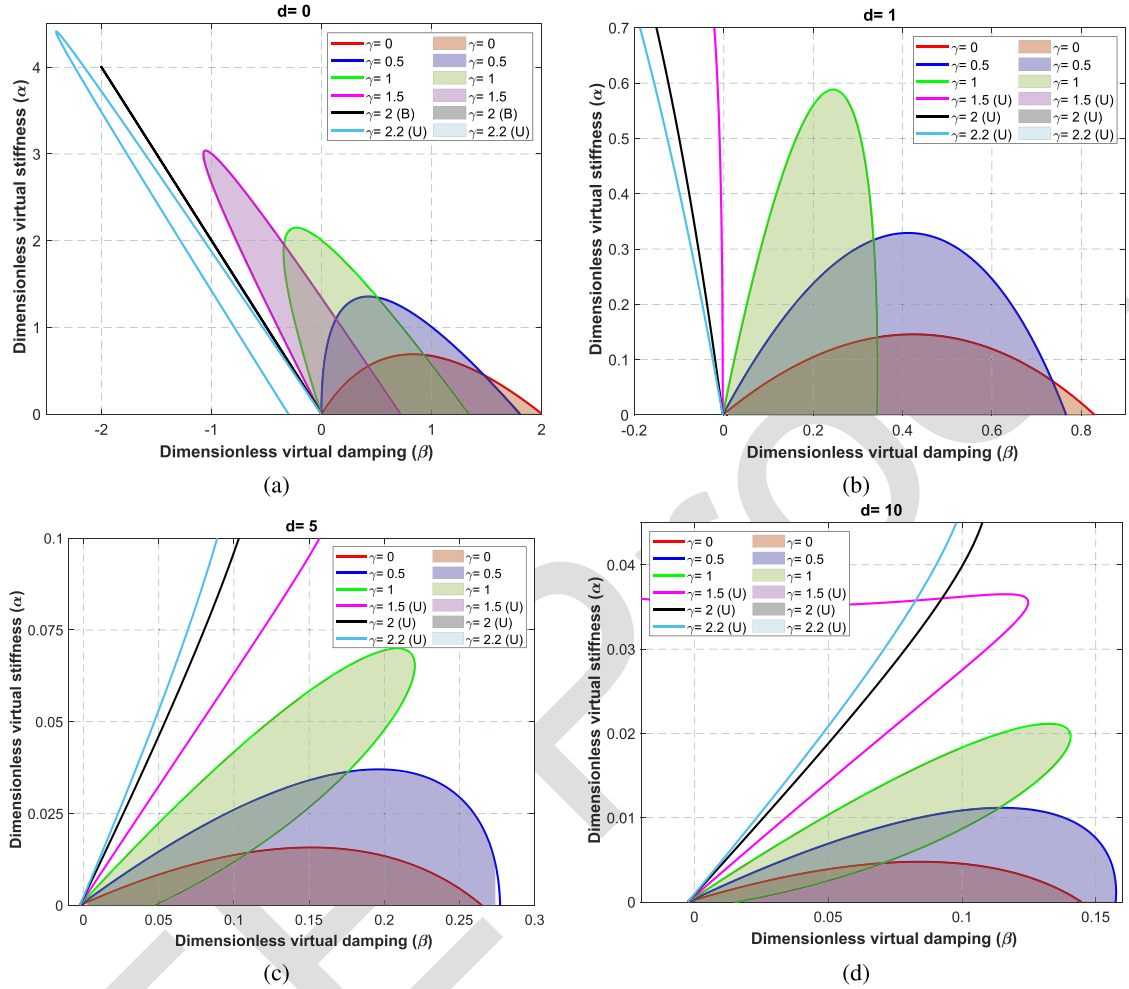

Fig. 8. The theoretical stability boundary (solid lines, determined from (7)) versus the stability region (highlighted areas), determined by simulation for $\gamma > 0$ and different time delays. The letter *U* stands for unstable case, and therefore, no stable region is found by simulations.

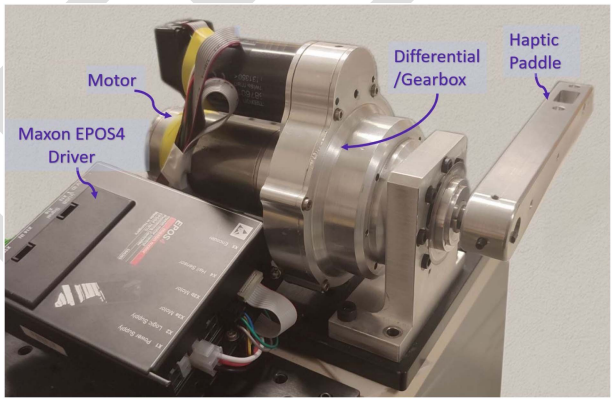

Fig. 9. Experimental haptic device.

experiments, a sampling rate of 1 kHz is used to read the paddle's angle, calculate velocity, and acceleration. A first-order low-pass filter with a 50 Hz cutoff frequency is used to attenuate measurement noise in velocity. Subsequently, the torque of the virtual object is calculated based on (1) and applied to the actuator by a Maxon EPOS4 70/15 driver. A fixed time delay of $T_d = 40$ ms was introduced in the experiments to prevent actuator saturation and protect the hardware from excessive stiffness and severe vibrations. As in other studies [10], [13], [19], the inclusion of a delay also captures its effect on system stability. Moreover, the delay was necessary to determine and plot the complete curved stability boundary; without it, only the linear portion of the curve could be obtained.

There is an internal PI controller in the MAXON drivers that operates at 25 kHz to track the applied torque. Experimental results indicated that the dynamics of the controller significantly impacted the stability boundaries. To ensure accurate validation, the effects of the PI controller, operating at a high frequency of 25 kHz, were included in both the simulations and the experimental analyses. Two different sets of PI controller parameters were tested. Lower PI gains were chosen to prevent high-frequency oscillations and ensure safe operation, though this approach led to slower torque tracking. In contrast, higher PI gains were used to improve torque tracking accuracy and achieve better alignment between experimental results and theoretical stability predictions. However, excessively high gains introduced instability and hardware-induced oscillations, highlighting the need for a conservative approach when selecting the

IEEE Transactions on Haptics (ToH) paper, presented at ICRA 2026, Vienna, Austria. Cite as ToH paper.

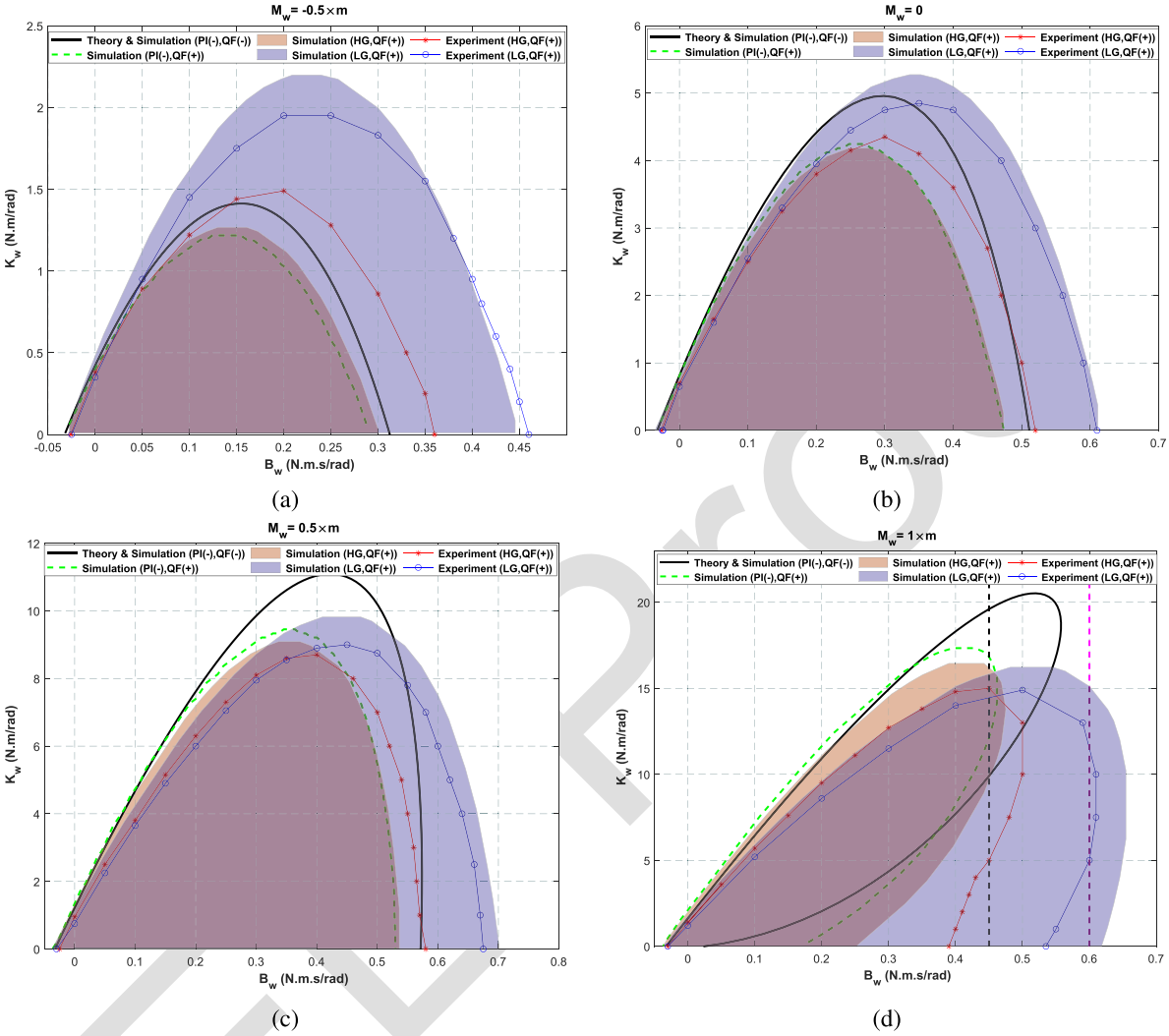

Fig. 10. The theoretical stability boundary (black solid line); stable region determined by simulations where the PI controller, quantization, and low-pass filter are omitted (PI(-), QF(-))—identical to the black solid line and therefore not plotted; stability boundary of simulations without the controller but with quantization and filter (PI(-), QF(+)) (green dashed line); stable region determined by simulations with high gains, including quantization and filter (HG, QF(+)) (pink region); stable region determined by simulations with low gains, including quantization and filter (LG, QF(+)) (blue region); experimental stability boundary for high gains (HG, QF(+)) (red stars); and experimental stability boundary for low gains (LG, QF(+)) (blue circles). Results are shown for (a) $M_w = -0.5$ m, (b) $M_w = 0$, (c) $M_w = 0.5$ m, and (d) $M_w = 1$ m. In all figures, the theoretical results are fully consistent with the simulation results obtained without the PI controller or without quantization and filtering. In subfigure (d), based on the vertical dashed black line at $B_w = 0.45$, a value of $5 < K_w < 15$ is required for stability in the high-gain case, while in the low-gain case, with $B_w = 0.60$, a value of $5 < K_w < 11$ is necessary for stability.

maximum allowable PI gains to avoid potential damage to the experimental setup. To account for the effect of the PI controller gains, two sets of experiments were performed. In the first set, the PI gains were selected to be low, as follows:

$$K_p = 600\,mV/A, \quad K_i = 600\,mV/(A.ms). \tag{16}$$

Meanwhile, in the second set, higher gains were used, as follows:

$$K_p = 6000\,mV/A, \quad K_i = 6000\,mV/(A.ms). \tag{17}$$

Thus, the label *low gain (LG)* refers to using the gains from (16), while the label *high gain (HG)* refers to the gains in (17). The PI controller parameters (K_p and K_i) in (16) and (17) are expressed in electrical units: K_p in mV/A (millivolts per ampere) and K_i in mV/(A · ms) (millivolts per ampere per millisecond). These units reflect the electrical nature of the system and are not directly convertible to mechanical units like Nm/s or N/m. These values and units are provided by the MAXON driver.

For a fair comparison, four simulation configurations were evaluated against the experimental data, as shown in Fig. 10, using the physical parameters mentioned above:

1) PI controller, quantization, and low-pass filter omitted. Since its stability boundary is identical to the theoretical one, no additional curve is plotted (labeled as *Theory and Simulation (PI(-), QF(-))*);
2) PI controller omitted, with quantization and low-pass filter included (labeled as *Simulation (PI(-), QF(+))*);
3) PI controller with high gains, with quantization and low-pass filter included (labeled as *Simulation (HG, QF(+))*);
4) Same as (3), but with low gains (labeled as *Simulation (LG, QF(+))*).

Throughout the experiments and simulations, various values of $\gamma = [-0.5, 0, 0.5, 1]$ were applied, while the sampling

time and time delay were set to $T = 1\,\text{ms}$ and $T_d = 40\,\text{ms}$, respectively.

VII. Results and Discussion

Fig. 10 compares the theoretical stability boundary derived from (7), the experimental stability boundaries obtained with varying PI controller gains, and the stable regions identified through different simulations.

In all subfigures, the simulation results of *PI(-), QF(-)* completely overlap with the theoretical stability boundary and are therefore not shown. All curves share approximately the same starting point on the (B_w, K_w) plane. Maximum of K_w obtained from the simulations of *PI(-), QF(+)* is lower than that of the corresponding theoretical results (black solid lines). In each case, both the *HG* and *LG* experiments yield higher values of B_w compared with the theoretical predictions. The maximum renderable B_w from the theoretical results is, however, closer to the experimental result of the *HG* case and also to the simulations including the PI controller with high gains. Furthermore, the *LG* cases—both in simulation and experiment—lead to wider stability regions (larger stable areas) compared with the *HG* cases. Additionally, simulations results of *PI(-), QF(+)*, is more similar to the results of *HG, QF(+)*, than *LG, QF(+)*.

In Fig. 10(a), corresponding to the case of negative virtual mass ($M_w = -0.5\,\text{m}$), the overall stability region becomes considerably smaller than in all other cases. This is also the only case in which the maximum experimental stiffness in both the HG and LG conditions exceeds the maximum theoretical value.

Fig. 10(b) corresponds to the case of zero virtual mass. There is good agreement between the simulation results of *PI(-), QF(+)* and *HG, QF(+)*. The maximum theoretical stiffness is closer to the experimental results of the *LG, QF(+)* case, while the maximum theoretical damping aligns more closely with the experimental results of the *HG, QF(+)* case.

In Fig. 10(c), a small difference can be observed between the maximum experimental stiffness in the *HG* and *LG* cases, whereas in (d), this difference is almost negligible. However, the maximum experimental damping in both (c) and (d) shows distinct differences between the *HG* and *LG* conditions.

This demonstrates that higher PI gains lead to a closer alignment of both experimental and simulation results with the theoretical predictions. The same trend is observed for other values of virtual mass in Fig. 10(b), (c), and (d).

In earlier sections, it was observed that, in certain scenarios, a minimum virtual spring value is required for stability. This behavior was previously noted in Fig. 8 across various time delays and virtual damping levels. The same phenomenon was evident in the experiments, as illustrated in Fig. 10(d).

For example, in the *low gain* case experimental results (depicted with blue circles), at $B_w = 0.6$ (vertical pink dashed line), the HD is unstable for $K_w < 5$, while at the same B_w, the HD becomes stable for $5 < K_w < 11$. This phenomenon is more pronounced with increasing PI-controller gains. In the *high gain* experiments (depicted by red stars), at $B_w = 0.45$ (vertical dashed black line), a minimum value of $K_w = 5$ is required for stability, more precisely, $5 < K_w < 15$.

During the experiments, no stability region was found for negative values of the virtual spring (i.e., $K_w < 0$). In all experiments, a small negative value of the virtual damping could be simulated, which is related to $B_{w_{\min}} = -bT/m$. From Fig. 10, it can be concluded that the stability equations determined in (7) predict the stability boundary with good accuracy.

The authors believe that increasing the controller gains improves the accuracy of predicting the theoretical stability boundary. However, during the experiments, a high-frequency noise, resembling an oscillatory or buzzing sound, was emitted from the Maxon drivers when the controller gains were set to very high values of $K_p = 9000\,\text{mV/A}$ and $K_i = 9000\,\text{mV/(A.ms)}$. To prevent potential damage, the maximum values of the controller gains were set below this limit, as specified in (17). When using gains of 6000, no such noise was observed.

In the conducted experiments under delayed conditions and high-gain control, without virtual mass ($\gamma = 0$), we measured $K_{\max}^{\text{exp}} = 4.3$ (theory: $K_{\max}^{\text{theo}} = 4.94$), whereas with virtual mass ($\gamma = 1$), we measured $K_{\max}^{\text{exp}} = 15$ (theory: $K_{\max}^{\text{theo}} = 20.35$). This corresponds to an increase of 412% in the theoretical prediction and 349% in the experimental implementation when virtual mass is introduced. Thus, the inclusion of virtual mass substantially enlarges the *achievable* stiffness region under delayed conditions, although the experimental values remain below the analytical bounds due to hardware non-idealities.

One important definition in haptic rendering is the stable area in the K_w-B_w plane, called *Z-width*, which was first defined by Colgate et al. in [28]. The larger the *Z-width*, the larger the stable region. Many researchers have suggested different methods for improving it, such as using active electrical damping [29], using magnetorheological fluids [30], using acceleration feedback [31], and using dual-rate haptic systems, which can help increase the velocity calculation accuracy at very high sampling rates [32], [33]. It has been shown that the velocity estimation method has a significant effect on *Z-width* [34] and can be limited due to the internal vibration modes of the HD [35].

The values of the maximum renderable virtual damping ($\beta_{\max}$), maximum renderable virtual spring ($\alpha_{\max}$), and the *Z-width* are plotted against values of $\gamma < 0$ (Fig. 11). The same plots can be seen in Fig. 12 for positive values of γ.

From Fig. 11, it can be seen that in the case of $\gamma < 0$, by reducing γ from 0 to -1, $\beta_{\max}$, $\alpha_{\max}$, and *Z-width* decrease continuously, regardless of the time delay. In the special case of $\gamma = -1$ (removing all effective mass from the HD), all of them are zero.

In the case of simulating positive values of γ, the behavior of the mentioned parameters is not the same. In the case of no time delay, the maximum renderable value of γ is 2 (Fig. 12(a)). In this figure, by increasing γ from 0 to 2, $\beta_{\max}$ decreases continuously, whereas in other time delays, first an increase is observed. In all time delays, $\alpha_{\max}$ increases, then decreases. The same also holds for the *Z-width*. Except in the case of $d = 0$, in all other time delays, the *Z-width* becomes zero while $\beta_{\max} \neq 0$ and $\alpha_{\max} \neq 0$ (unlike Fig. 11, which was for $\gamma < 0$). This can be described as closing the stability curve, which causes a zero value of the *Z-width* and nonzero values for $\alpha_{\max}$ and $\beta_{\max}$ (like the case of $\gamma = 2$ in Fig. 7).

IEEE Transactions on Haptics (ToH) paper, presented at ICRA 2026, Vienna, Austria. Cite as ToH paper.

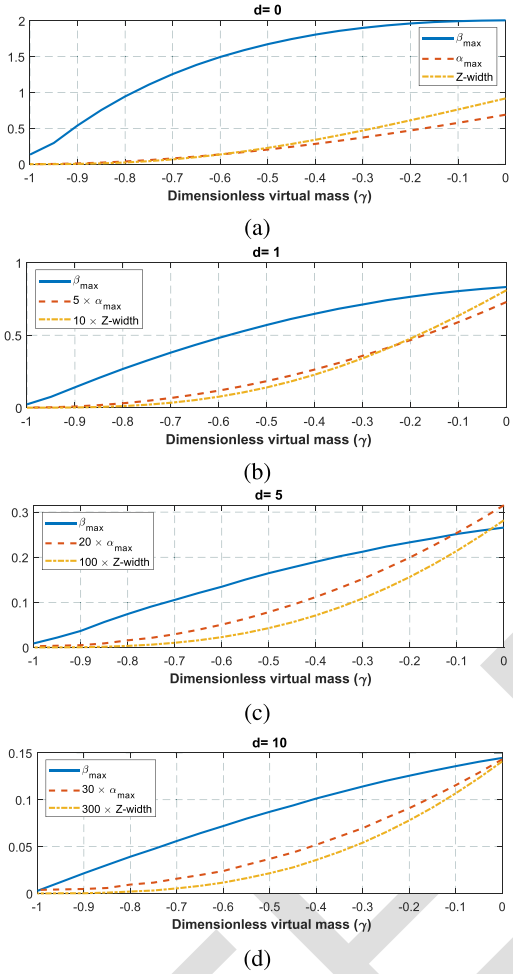

Fig. 11. Values of the maximum renderable virtual damping ($\beta_{\max}$) (solid blue line), maximum renderable virtual spring ($\alpha_{\max}$) (dashed red line), and the *Z-width* (dotted orange line) versus negative values of the dimensionless virtual mass (γ), in the case of: (a) $d = 0$, (b) $d = 1$, (c) $d = 5$, and (d) $d = 10$.

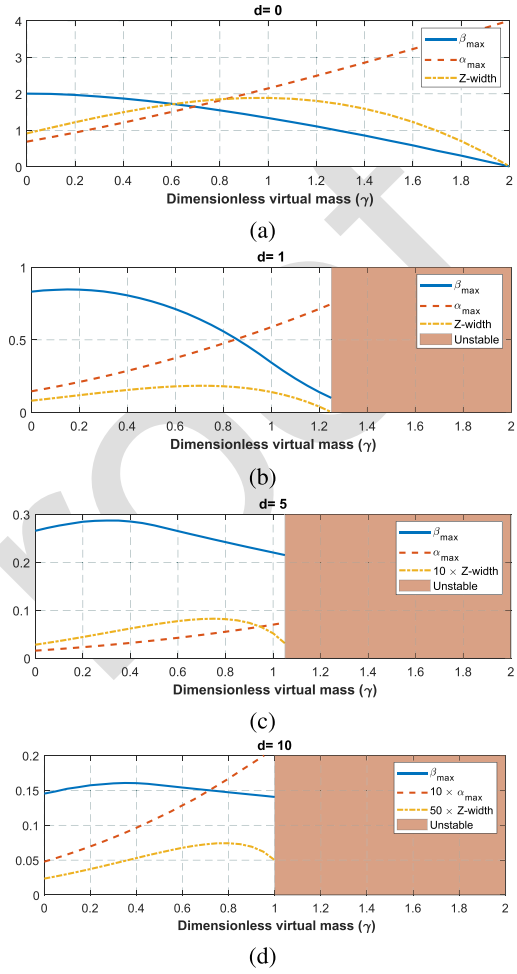

Fig. 12. Values of the maximum renderable virtual damping ($\beta_{\max}$) (solid blue line), maximum renderable virtual spring ($\alpha_{\max}$) (dashed red line), and the *Z-width* (dotted orange line) versus positive values of the dimensionless virtual mass (γ), in the case of: (a) $d = 0$, (b) $d = 1$, (c) $d = 5$, and (d) $d = 10$. The red region stands for instability.

It should be mentioned that the perceived discontinuity in $\beta_{\max}$, $\alpha_{\max}$, and *Z-width* at $\gamma = 0$ between Figs. 11 and 12 is solely due to the application of different uniform scaling factors in these figures to enhance the visibility of very small stability limit values. The underlying non-dimensional values of $\beta_{\max}$, $\alpha_{\max}$, and *Z-width* are, in fact, smooth and continuous through $\gamma = 0$ in both the simulations and the experimental data.

The current study provides valuable insights into the stability of haptic devices when simulating virtual environments with mass, spring, and damper elements. However, several limitations should be acknowledged. First, the haptic device is modeled as a 1-DOF system with effective mass, viscous friction, and Coulomb friction. This simplification, while useful for stability analysis, may not capture the full complexity of multi-DOF haptic devices. Second, the experiments employed a fixed time delay of 40 ms to safeguard against excessive rendered stiffness and potential hardware damage. While this delay is needed for safety, it may not reflect the full range of delays encountered in different operational scenarios. Additional limitations include the selection of PI controller gains, which were chosen to balance stability and performance.

VIII. Conclusion and Future Work

This study conducted a stability analysis of a one-degree-of-freedom (1-DOF) haptic device by modeling the virtual environment as a combination of a mass, spring, and damper. The analysis resulted in closed-form equations that define the relationships among the virtual mass, spring, and damper, along with other system parameters, at the stability boundary. Unlike previous works that relied on iterative trial-and-error searches, the present formulation provides explicit closed-form expressions, including for $\theta_{\max}$, allowing stability boundaries to be generated efficiently. It was also established that the minimum virtual damping is always $B_{w,\min} = -b$, independent of time delay or virtual mass.

In the absence of time delay ($d = 0$), the analysis showed that properly tuning the virtual damping and virtual mass can increase the maximum renderable stiffness by up to 5.8 times in theory. These findings are consistent with the reviewed studies when formulations are extended and numerical iterations are applied to find the maximum renderable value of α.

When a time delay was included ($d = 40$), both simulations and experiments confirmed that adding virtual mass enlarges the achievable stiffness region, with experiments demonstrating an increase of about 3.5 times (from $K_{\max}^{\text{exp}} = 4.3$ to 15), consistent with the theoretical prediction of approximately 4.1 times (from $K_{\max}^{\text{theo}} = 4.94$ to 20.35).

Additionally, a new behavior was identified: in certain cases, a nonzero minimum virtual spring value is required for stability. This behavior can also be reproduced by extending previous work to a wider range of virtual-environment parameters. All of these phenomena were validated through both simulations and experiments, confirming that the results of earlier studies represent special cases of the more general framework presented here.

As shown in this paper, when either the time delay or the virtual mass was zero, closed-form equations for $\theta_{\max}$ were derived. In the general case, where both time delay and virtual damping are present, $\theta_{\max}$ was determined numerically within known bounds. As part of future work, deriving closed-form expressions for this general case is proposed. Also, two additional theoretical aspects could be explored in greater depth: providing a more rigorous analytical proof of the necessity of $\alpha > 0$, and fully characterizing why the "left-sided" stability curves do not correspond to stable regions. One promising direction to investigate these questions is to perform a root-locus analysis of the closed-loop system to examine how the poles migrate as the system parameters vary.

APPENDIX

A. The Real and Imaginary Parts of the Characteristic Equation

The real and imaginary parts of the characteristic equation are given as follows:

$$\begin{aligned}
\mathit{Real\,part} = & -\delta^2\,(1+\Gamma)\cos\left(\theta\ (d+3)\right)\\
& +\delta^2\cos\left(\theta\ (d+2)\right)+\delta^2\Gamma\cos\left(\theta\ (d+4)\right)\\
& +\left(\left(\left(-\beta-2\,\alpha+3\right)\gamma+2\,\beta+\alpha\right)\Gamma\right.\\
& +\left(-\beta-\alpha-\gamma-2\right)\delta-\alpha-3\,\gamma\big)\cos\left(2\,\theta\right)\\
& +\left(\left(\left(\beta+\alpha-\gamma-1\right)\delta-\alpha-\gamma\right)\Gamma\right.\\
& \left.+\alpha+\delta+\gamma\right)\cos\left(3\,\theta\right)\\
& +\left(\left(\left(\alpha-3\right)\gamma-\beta\right)\Gamma+\left(2\,\gamma+1\right)\delta\right.\\
& \left.+\gamma\ (\beta+3)\right)\cos\left(\theta\right)\\
& +\gamma\ (\Gamma-\delta-1)=0, \qquad (18)\\
\mathit{Imag\,part} = & -\delta^2\,(1+\Gamma)\sin\left(\theta\ (d+3)\right)\\
& +\delta^2\sin\left(\theta\ (d+2)\right)+\delta^2\Gamma\sin\left(\theta\ (d+4)\right)\\
& +\left(\left(\left(-\beta-2\,\alpha+3\right)\gamma+2\,\beta+\alpha\right)\Gamma\right.\\
& +\left(-\beta-\alpha-\gamma-2\right)\delta-\alpha-3\,\gamma\big)\sin\left(2\,\theta\right)\\
& +\left(\left(\left(\beta+\alpha-\gamma-1\right)\delta-\alpha-\gamma\right)\Gamma\right.\\
& \left.+\alpha+\delta+\gamma\right)\sin\left(3\,\theta\right)\\
& -\sin\left(\theta\right)\left(\left(\left(-\alpha+3\right)\gamma+\beta\right)\Gamma\right.\\
& \left.+\left(-2\,\gamma-1\right)\delta-\gamma\ (\beta+3)\right)=0. \qquad (19)
\end{aligned}$$

B. Defined Parameters and Coefficients

Using $\delta = bT/m$ and $\Gamma = e^{\delta}$, parameters and coefficients used in (7) are as follows:

$$K_1 = 32\,\sin^5\left(\tfrac{\theta}{2}\right)\cos\left(\tfrac{\theta}{2}\right), \qquad (20)$$

$$K_2 = (1-\Gamma)^2, \qquad (21)$$

$$K_3 = 1+\Gamma^2-2\Gamma\cos(\theta), \qquad (22)$$

$$K_4 = 1+\Gamma+\Gamma^2. \qquad (23)$$

Using the aforementioned definitions, the coefficients of C_1 to C_{11} are defined as follows:

$$C_1 = K_1\,K_2, \qquad (24)$$

$$C_2 = -2\,K_3\,\sin(\theta)\,(\cos(\theta)-1), \qquad (25)$$

$$C_3 = -16\,\sin\left(\frac{\theta}{2}\right)^4\sin(\theta)\,(\Gamma^2-1), \qquad (26)$$

$$\begin{aligned}
C_4 = {} & K_4\,(2\sin(\theta(d+1))-\sin(d\theta)-\sin(\theta(d+2)))\\
& -4\,\Gamma\,\sin(\theta(d+1))\,\sin\left(\frac{\theta}{2}\right)\sin\left(\frac{3\theta}{2}\right), \qquad (27)
\end{aligned}$$

$$\begin{aligned}
C_5 = {} & -8\,\sin\left(\frac{\theta}{2}\right)^3(\Gamma-1)\\
& \times\left(\cos\left(\frac{\theta(2d+1)}{2}\right)-\Gamma\,\cos\left(\frac{\theta(2d+3)}{2}\right)\right), \qquad (28)
\end{aligned}$$

$$C_6 = -2\,K_2\,\sin(\theta)\,(\cos(\theta)-1), \qquad (29)$$

$$C_7 = K_3\,\sin(\theta), \qquad (30)$$

$$C_8 = \sin(\theta)\,\left(2(\Gamma^2-1)\right)\,(\cos(\theta)-1), \qquad (31)$$

$$C_9 = K_1\,(\Gamma^2-1), \qquad (32)$$

$$\begin{aligned}
C_{10} = {} & -2\,\cos\left(\frac{\theta(2d+1)}{2}\right)\\
& \times\left(K_4\,\sin\left(\frac{\theta}{2}\right)-\Gamma\,\sin\left(\frac{3\theta}{2}\right)\right), \qquad (33)
\end{aligned}$$

$$\begin{aligned}
C_{11} = {} & 4\,\sin\left(\frac{\theta}{2}\right)^2\left(\Gamma^2\,\sin(\theta+d\theta)+\sin(d\theta)\right)\\
& -4\,\Gamma\,\sin\left(\frac{\theta}{2}\right)\sin\left(\frac{\theta}{2}+d\theta\right)\sin(\theta). \qquad (34)
\end{aligned}$$

C. Case $d = 0$, γ Arbitrary: Closed-Form Expression for $\theta_{\max}$

For the case $d = 0$, when plotting the stability boundaries using (7) of the manuscript, θ varies between a minimum ($\theta_{\min}$) and a maximum ($\theta_{\max}$). In this subsection, it is demonstrated that $\theta_{\min} = 0$, and expressions are derived to determine $\theta_{\max}$. Set the half–angle shorthands

$$s_h := \sin\left(\tfrac{\theta}{2}\right), \qquad c_h := \cos\left(\tfrac{\theta}{2}\right), \qquad c := \cos\theta, \qquad (35)$$

IEEE Transactions on Haptics (ToH) paper, presented at ICRA 2026, Vienna, Austria. Cite as ToH paper.

so that $\sin\theta = 2s_h c_h$, $\cos\theta - 1 = -2s_h^2$, and $\cos(\frac{3\theta}{2}) = 4c_h^3 - 3c_h$. For $d = 0$, the $\theta_{\max}$ will vanish the following equation (numinator of α's fraction):

$$\Phi(\theta) = \gamma C_1(\theta) + \gamma\delta^2 C_2(\theta) + \gamma\delta C_3(\theta) + \delta^3 C_4(\theta) + \delta^2 C_5(\theta) = 0. \quad (36)$$

In the case of $d = 0$, each term can be simplified as:

$$C_1 = K_2\, K_1 = 32\, K_2\, s_h^5 c_h, \quad (37)$$

$$C_2 = -2K_3 \sin\theta\,(\cos\theta - 1) = 8\, K_3\, s_h^3 c_h, \quad (38)$$

$$C_3 = -16\, s_h^4 \sin\theta\,(\Gamma^2 - 1) = -32(\Gamma^2 - 1)\, s_h^5 c_h, \quad (39)$$

$$C_4 = K_4\big(2\sin\theta - \sin 2\theta\big) - 4\Gamma\, \sin\theta\, s_h\, \sin\big(\tfrac{3\theta}{2}\big) = 8\, s_h c_h\Big[(K_4 - 3\Gamma)s_h^2 + 4\Gamma s_h^4\Big], \quad (40)$$

$$C_5 = -8\, s_h^3(\Gamma - 1)\big(c_h - \Gamma\cos\big(\tfrac{3\theta}{2}\big)\big) = 8\, s_h^3 c_h\Big[K_2 - 4\Gamma(\Gamma - 1)s_h^2\Big]. \quad (41)$$

Introduce the nonnegative variable

$$u := 1 - \cos\theta = 2s_h^2 \in [0, 2]. \quad (42)$$

With $c = 1 - u$ one has $K_3 = K_2 + 2\Gamma u$ and $K_4 - 3\Gamma = K_2$. Substitution into $\Phi(\theta)$ and factoring $8s_h c_h$ yields

$$\Phi(\theta) = 8\, s_h c_h u \left(A\, u + \frac{1}{2} K_2\, \delta^2(\gamma + 1 + \delta)\right), \quad (43)$$

where

$$A = \gamma\left[(1 - \Gamma)^2 - \delta(\Gamma^2 - 1) + \Gamma\delta^2\right] + \Gamma\delta^2(1 - \Gamma + \delta). \quad (44)$$

The prefactor $8s_h c_h$ vanishes only at $\theta \in \{0, \pi\}$; simply shows that while plotting stability curves, θ should start from $\theta_{\min} = 0$. Excluding the trivial root $u = 0$ ($\theta = 0$), the nontrivial branch solves

$$A\, u + \frac{1}{2} K_2\, \delta^2(\gamma + 1 + \delta) = 0, \quad (45)$$

hence

$$u = -\frac{K_2\, \delta^2(\gamma + 1 + \delta)}{2A}, \qquad 0 \le u \le 2. \quad (46)$$

Recovering the angle from $u = 1 - \cos\theta$ is most stable via the half–angle map

$$\theta_{\max} = 2\arctan\sqrt{\frac{u}{2 - u}}, \quad (47)$$

with the usual clipping of u into [0,2] in floating-point arithmetic. This expression provides a closed form for $\theta_{\max}$ in the case $d = 0$, $\gamma \neq 0$, and retains the exact dependence on $\Gamma = e^{\delta}$.

D. Case $\gamma = 0$, d Arbitrary: Closed-Form Expression for $\theta_{\max}$

In the case of $\gamma = 0$, while plotting the stability boundaries using (7) of the manuscript, θ should vary between a minimum ($\theta_{\min}$) and a maximum ($\theta_{\max}$). In this subsection, it is shown that $\theta_{\min} = 0$, and expressions are derived to determine $\theta_{\max}$.

Minimum and maximum values of θ occur when $\alpha = 0$. With $\gamma = 0$, this condition becomes

$$\delta\, C_4(\theta) + C_5(\theta) = 0. \quad (48)$$

Using the identity $\sin(x + \theta) - 2\sin x + \sin(x - \theta) = -4\sin^2(\frac{\theta}{2})\sin x$, and standard sum–to–product/half–angle formulas, the left-hand side can be written *exactly* as

$$\Phi(\theta) = A_S(\theta)\, \sin((d{+}1)\theta) + A_D(\theta)\, \sin(d\theta) = 0, \quad (49)$$

where we set

$$sh := \sin\frac{\theta}{2}, ch := \cos\frac{\theta}{2}, s := \sin\theta, c := \cos\theta, \Gamma = e^{\delta}, \quad (50)$$

and

$$A_S(\theta) = \delta\, B(\theta) - 4\, sh^2\,(\Gamma - 1)\,\big(1 + \Gamma - 2\Gamma c\big), \quad (51)$$

$$A_D(\theta) = -4\, sh^2\,(\Gamma - 1)^2, \quad (52)$$

$$B(\theta) = 2\Big(\Gamma^2 + 1 - (\Gamma + 1)^2\, c + 2\Gamma\, c^2\Big). \quad (53)$$

The trivial root $\theta = 0$ is always present, hence $\theta_{\min} = 0$. We therefore seek the *smallest positive nontrivial* solution, denoted $\theta_{\max}$. The term $\sin((d{+}1)\theta)$ carries the leading oscillation. A natural expansion point is where this term is stationary, so that small changes in θ do not immediately change its contribution and the balance with the secondary harmonic $\sin(d\theta)$ can occur locally. Imposing stationarity,

$$\frac{d}{d\theta}\sin((d{+}1)\theta) = (d{+}1)\cos((d{+}1)\theta) = 0, \quad (54)$$

yields $\cos((d{+}1)\theta) = 0$ and therefore the grid

$$\theta = \frac{(2k{+}1)\pi}{2(d{+}1)}, \qquad k \in Z. \quad (55)$$

Selecting the first positive instance gives

$$\theta_0 = \frac{\pi}{2(d{+}1)}. \quad (56)$$

At this angle $\sin((d{+}1)\theta_0) = 1$, and the companion harmonic is nondegenerate in value and slope:

$$\sin(d\theta_0) = \cos\Big(\tfrac{\pi}{2(d+1)}\Big) > 0, \cos(d\theta_0) = \sin\Big(\tfrac{\pi}{2(d+1)}\Big) > 0. \quad (57)$$

A Taylor expansion with $\theta = \theta_0 + \eta$ gives $\sin((d{+}1)\theta) = 1 + O(\eta^2)$ and $\sin(d\theta) = \sin(d\theta_0) + d\,\eta\,\cos(d\theta_0) + O(\eta^2)$. Thus, the balance $\Phi(\theta) = 0$ is achieved by a small linear correction η, and the true root lies close to θ_0.

A single Newton update from θ_0 provides an accurate approximation to the smallest positive root:

$$\theta_{\max} \approx \theta_0 - \frac{\Phi(\theta_0)}{\Phi'(\theta_0)}, \quad (58)$$

where

$$\Phi'(\theta) = A_S'(\theta)\, \sin((d{+}1)\theta) + A_S(\theta)\,(d{+}1)\cos((d{+}1)\theta) + A_D'(\theta)\, \sin(d\theta) + A_D(\theta)\, d\cos(d\theta), \quad (59)$$

and

$$A'_S(\theta) = \delta\, B'(\theta) - 4(\Gamma-1)\left(\tfrac{s}{2}\,(1+\Gamma-2\Gamma c) + 2\Gamma s h^2\, s\right), \tag{60}$$

$$A'_D(\theta) = -\,2(\Gamma-1)^2\, s, \tag{61}$$

$$B'(\theta) = 2s\Big((\Gamma+1)^2 - 4\Gamma c\Big). \tag{62}$$

Evaluating $\Phi(\theta_0)$ and $\Phi'(\theta_0)$ at $\theta = \theta_0$ yields the compact expression

$$\theta_{\max} = \theta_0 - \frac{A_{S0} + A_{D0}\cos(\theta_0)}{A'_{S0} + A'_{D0}\cos(\theta_0) + d\, A_{D0}\sin(\theta_0)}, \tag{63}$$

where $A_{S0}, A_{D0}, A'_{S0}, A'_{D0}$ denote the values of $A_S(\theta), A_D(\theta), A'_S(\theta), A'_D(\theta)$ evaluated at $\theta = \theta_0$. This final form corresponds to the expression reported in the main text.

E. The Starting Point and Sign of α Near $\theta = 0$

In this subsection, the starting point and initial sign of the stability curves are determined. Since this point corresponds to values of θ near zero, the asymptotic behavior of the coefficients K_i and C_i can be approximated by their leading-order terms in the Taylor expansions. Specifically, K_i and C_i behave as constant coefficients multiplied by powers of θ:

$$K_1 \approx 16\,\theta^5, \qquad K_2 = (1-\Gamma)^2,$$
$$K_3 = 1 + \Gamma^2 - 2\Gamma\cos(\theta), \qquad K_4 = 1 + \Gamma + \Gamma^2. \tag{64}$$

Using these definitions, the coefficients C_i can be approximated as

$$\begin{aligned}
&C_1 \approx K_2\, K_1 \approx (\text{const})\,\theta^5, && C_2 \approx K_3\,(\text{const})\,\theta^3,\\
&C_3 \approx (\Gamma^2-1)\,(\text{const})\,\theta^5, && C_4 \approx \Delta\,\theta^3,\\
&C_5 \approx \eta\,\theta^3, && C_6 \approx K_2\,(\text{const})\,\theta^3,\\
&C_7 \approx K_3\,(\text{const})\,\theta, && C_8 \approx (\Gamma^2-1)\,(\text{const})\,\theta^3,\\
&C_9 \approx (\Gamma^2-1)\,(\text{const})\,\theta^5, && C_{10} \approx (3\Gamma - K_4)\,(\text{const})\,\theta,\\
&C_{11} \approx \xi\,\theta^3.
\end{aligned} \tag{65}$$

By substituting these approximations into (7), the dimensionless virtual stiffness α can be expressed as

$$\alpha = \frac{\gamma C_1 + \gamma\delta^2 C_2 + \gamma\delta C_3 + \delta^3 C_4 + \delta^2 C_5}{C_6 + \delta^2 C_7 + \delta C_8}. \tag{66}$$

For small values of θ, the leading-order terms of the numerator and denominator give

$$\alpha(\theta) \approx \frac{(\gamma\delta^2 K_3 + \delta^3\Delta + \delta^2\eta)\,\theta^3}{K_2\,\theta^3 + \delta^2 K_3\,\theta + \delta(\Gamma^2-1)\,\theta^3}. \tag{67}$$

Since all coefficients $\delta > 0$, $K_2 = (1-\Gamma)^2 > 0$, $K_3 \geq 0$, and $\Gamma = e^{\delta} > 1$, both the numerator and denominator are positive for small positive θ. Therefore,

$$\lim_{\theta\to 0^+} \alpha(\theta) = 0^+. \tag{68}$$

For completeness, the asymptotic behavior of β is obtained from (8):

$$\beta = \frac{-\gamma C_1 - \gamma\delta^2 C_2 + \gamma\delta C_9 + \delta^3 C_{10} + \delta^2 C_{11}}{C_6 + \delta^2 C_7 + \delta C_8}. \tag{69}$$

Neglecting higher-order terms yields

$$\lim_{\theta\to 0} \beta = -\delta, \tag{70}$$

confirming that all stability boundaries originate from $(B_w, K_w) = (-b, 0)$ or in dimensionless form, $(\beta, \alpha) = (-\delta, 0)$. This implies that all stability curves start from the point $(\beta, \alpha) = (-\delta, 0)$, and as θ increases from zero, α becomes positive, indicating that negative stiffness values ($\alpha < 0$) always correspond to unstable configurations. Hence, the small-angle expansion not only determines the common starting point of all stability curves but also analytically confirms that the stability boundary initially lies in the region $\alpha > 0$; therefore, positive stiffness ($\alpha > 0$) is a necessary condition for stability.

References

[1] M. Khan et al., "Wearable haptics for orthotropic actuation based on perpendicularly nested auxetic SMA knotting," *Adv. Mater.*, vol. 37, no. 1, 2025, Art. no. 2411353.

[2] C. Cuan, A. Okamura, and M. Khansari, "Leveraging haptic feedback to improve data quality and quantity for deep imitation learning models," *IEEE Trans. Haptics*, vol. 17, no. 4, pp. 984–991, Oct.–Dec. 2024.

[3] C. Hutchison, J. Hewlett, S. Arbatani, A. Weill-Duflos, and J. Kovecses, "Haptic interactions subject to variable latency," *IEEE Trans. Haptics*, vol. 17, no. 1, pp. 66–71, Jan.–Mar. 2024.

[4] K.-H. Lee, H. Singh, T. Hulin, and J.-H. Ryu, "Simultaneous use of autonomy guidance haptic feedback and obstacle avoiding force feedback for mobile robot teleoperation," in *Proc. 22nd Int. Conf. Control, Automat. Syst.*, 2022, pp. 978–981.

[5] A. Pervez, A. Ali, J.-H. Ryu, and D. Lee, "Novel learning from demonstration approach for repetitive teleoperation tasks," in *Proc. 2017 IEEE World Haptics Conf.*, 2017, pp. 60–65.

[6] J. J. Gil, A. Ugartemendia, and I. Diaz, "Stability analysis and user perception of haptic rendering combining virtual elastic, viscous and inertial effects," *Appl. Sci.*, vol. 10, no. 24, 2020, Art. no. 8807.

[7] H. Choi, N. G. Kim, A. Jafari, H. Singh, and J.-H. Ryu, "Virtual inertia as an energy dissipation element for haptic interfaces," *IEEE Robot. Automat. Lett.*, vol. 7, no. 2, pp. 2708–2715, Apr. 2022.

[8] L. Pecly and K. Hashtrudi-Zaad, "Uncoupled stability of kinesthetic haptic systems simulating mass-damper-spring environments with complementary filter," in *Proc. 2022 IEEE/ASME Int. Conf. Adv. Intell. Mechatron.*, 2022, pp. 97–102.

[9] A. Mashayekhi, A. Karami, and B. Siciliano, "A new approach for simplifying multi-degree of freedom haptic device dynamics model," *J. Intell. Robotic Syst.*, vol. 108, no. 1, 2023, Art. no. 4.

[10] A. Karami and A. Mashayekhi, "Improving haptic device stability through redundancy resolution," in *Proc. 10th RSI Int. Conf. Robot. Mechatron.*, 2022, pp. 527–532.

[11] N. Diolaiti, G. Niemeyer, F. Barbagli, and J. K. Salisbury, "Stability of haptic rendering: Discretization, quantization, time delay, and coulomb effects," *IEEE Trans. Robot.*, vol. 22, no. 2, pp. 256–268, Apr. 2006.

[12] A. Mashayekhi, R. B. Boozarjomehry, A. Nahvi, A. Meghdari, and P. Asgari, "Improved passivity criterion in haptic rendering: Influence of coulomb and viscous friction," *Adv. Robot.*, vol. 28, no. 10, pp. 695–706, 2014.

[13] J. J. Abbott and A. M. Okamura, "Effects of position quantization and sampling rate on virtual-wall passivity," *IEEE Trans. Robot.*, vol. 21, no. 5, pp. 952–964, Oct. 2005.

[14] J. J. Gil, A. Avello, A. Rubio, and J. Florez, "Stability analysis of a 1 dof haptic interface using the routh-hurwitz criterion," *IEEE Trans. Control Syst. Technol.*, vol. 12, no. 4, pp. 583–588, Jul. 2004.

[15] A. Mashayekhi, S. Behbahani, F. Ficuciello, and B. Siciliano, "Influence of human operator on stability of haptic rendering: A closed-form equation," *Int. J. Intell. Robot. Appl.*, vol. 4, no. 4, pp. 403–415, 2020.

IEEE Transactions on Haptics (ToH) paper, presented at ICRA 2026, Vienna, Austria. Cite as ToH paper.

[16] J. E. Speich, L. Shao, and M. Goldfarb, "Modeling the human hand as it interacts with a telemanipulation system," *Mechatronics*, vol. 15, no. 9, pp. 1127–1142, 2005.

[17] J. J. Gil, A. Ugartemendia, and I. Dıáz, "Rendering virtual inertia in haptic interfaces: Analysis and limitations," in *Proc. 2022 Int. Conf. Robot. Automat.*, 2022, pp. 8876–8881.

[18] T. Hulin, A. Albu-Schäffer, and G. Hirzinger, "Passivity and stability boundaries for haptic systems with time delay," *IEEE Trans. Control Syst. Technol.*, vol. 22, no. 4, pp. 1297–1309, Jul. 2014.

[19] J. J. Gil, E. Sánchez, T. Hulin, C. Preusche, and G. Hirzinger, "Stability boundary for haptic rendering: Influence of damping and delay," *J. Comput. Inf. Sci. Eng.*, vol. 9, no. 1, 2009.

Q6 [20] N. Colonnese and A. M. Okamura, "M-width: Stability, noise characterization, and accuracy of rendering virtual mass," *Int. J. Robot. Res.*, vol. 34, no. 6, pp. 781–798, 2015.

[21] I. Desai, A. Gupta, and D. Chakraborty, "Virtual mass feedback for rendering stiff virtual springs," in *Proc. 2019 IEEE World Haptics Conf.*, 2019, pp. 211–216.

[22] M. Hejrati and J. Mattila, "Nonlinear subsystem-based adaptive impedance control of physical human-robot-environment interaction in contact-rich tasks," 2023, *arXiv:2303.01397*.

Q7 [23] H. K. Khalil, *Control of Nonlinear Systems*. Englewood Cliffs, NJ, USA: Prentice-Hall, 2002.

[24] A. Mashayekhi, S. Behbahani, F. Ficuciello, and B. Siciliano, "Analytical stability criterion in haptic rendering: The role of damping," *IEEE/ASME Trans. Mechatron.*, vol. 23, no. 2, pp. 596–603, Apr. 2018.

[25] A. Mashayekhi, S. Behbahani, F. Ficuciello, and B. Siciliano, "Delay-dependent stability analysis in haptic rendering," *J. Intell. Robotic Syst.*, vol. 97, pp. 33–45, 2020.

[26] A. Khorasani et al., "Mitigating collision forces and improving response performance in human-robot interaction by using dual-motor actuators," *IEEE Robot. Automat. Lett.*, vol. 9, no. 6, pp. 5982–5989, Jun. 2024.

[27] A. Mashayekhi, O. Akhif, A. Khorasani, and T. Verstraten, "Stability analysis of a dual-rate haptic system: A new closed-form solution," *IEEE Robot. Automat. Lett.*, vol. 10, no. 6, pp. 6472–6479, Jun. 2025.

[28] J. E. Colgate and J. M. Brown, "Factors affecting the z-width of a haptic display," in *Proc. 1994 IEEE Int. Conf. Robot. Automat.*, 1994, vol. 4, pp. 3205–3210.

[29] D. W. Weir, J. E. Colgate, and M. A. Peshkin, "Measuring and increasing z-width with active electrical damping," in *Proc. 2008 Symp. Haptic Interfaces Virtual Environ. Teleoperator Syst.*, 2008, pp. 169–175.

[30] X. Yin, C. Wu, S. Wen, and J. Zhang, "Smart design of z-width expanded thumb haptic interface using magnetorheological fluids," *IEEE Trans. Instrum. Meas.*, vol. 70, 2021, Art. no. 7504111.

[31] N. Yasrebi and D. Constantinescu, "Extending the z-width of a haptic device using acceleration feedback," in *Proc. Haptics: Percep., Devices Scenarios: 6th Int. Conf.*, Madrid, Spain, Jun. 2008, pp. 157–162.

[32] M. H. Koul, M. Manivannan, and S. K. Saha, "Enhancing the z-width of haptics interfaces through dual-rate sampling," in *Proc. Conf. Adv. Robot.*, 2013, pp. 1–6.

[33] A. R. Tiwari, S. Saha, and S. Kumar, "Improved dual haptic controller with extra virtual damper for z-width enhancement," in *Proc. 3rd Int. Conf. Intell. Comput. Instrum. Control Technol.*, 2022, pp. 78–81.

[34] V. Chawda, O. Celik, and M. K. O'Malley, "Evaluation of velocity estimation methods based on their effect on haptic device performance," *IEEE/ASME Trans. Mechatron.*, vol. 23, no. 2, pp. 604–613, Apr. 2018.

[35] J. J. Gil, M. J. Puerto, I. Dıáz, and E. Sánchez, "On the z-width limitation due to the vibration modes of haptic interfaces," in *Proc. 2010 IEEE/RSJ Int. Conf. Intell. Robots Syst.*, 2010, pp. 5054–5059.

Ahmad Mashayekhi is currently a Postdoctoral Researcher with the Robotics & Multibody Mechanics Research Group (R & MM) of the Vrije Universiteit Brussel, Ixelles, Belgium. He was a Researcher with the PRISMA Lab (Italy) in 2016–2017. His main research interests include stability and transparency analysis of haptic systems, friction modeling, human–robot interaction, numerical optimization, metaheuristic algorithms, and, more recently, machine-learning algorithms for 3D object detection inside point clouds.

Mehdi Shakeri received the B.Sc. degree in mechanical engineering from Isfahan University, Isfahan, Iran, in 2014, and the M.Sc. degree in mechanical engineering from the Isfahan University of Technology, Isfahan, in 2018. He is currently working toward the Ph.D. degree the University of Regina, Regina, SK, Canada. He was a Research Assistant in the Advanced Robotics and Mechatronics Laboratory with the Isfahan University of Technology. His current research interests include control, robotics, and haptics.

Amin Khorasani received the M.Sc. degree in mechatronics in 2015, with a main focus on parallel robots and haptic system design for robotic eye surgery, with a background in mechanical engineering. He is currently the Ph.D. Researcher with Vrije Universiteit Brussel, Ixelles, Belgium, where his research is focuses on efficient and safe actuator development for human-centred robotics.

Tom Verstraten (Member, IEEE) is currently a Professor with the Robotics & Multibody Mechanics Research Group (R & MM) of the Vrije Universiteit Brussel, Ixelles, Belgium. He was a Visiting Researcher with TU Darmstadt Darmstadt, Germany, in 2017 His main research interests include study and development of energy-efficient actuation systems for robotic prostheses, exoskeletons, and collaborative robots. He was awarded a Fulbright grant for visiting scholars for a research stay with the University of Tulsa, Tulsa, OK, USA, in 2018-19.